Revealing mesoscopic structural universality with diffusion

Dmitry S. Novikov[a,1], Jens H. Jensen[b], Joseph A. Helpern[b], and Els Fieremans[a]

[a]Bernard and Irene Schwartz Center for Biomedical Imaging, Department of Radiology, New York University School of Medicine, New York, NY 10016; and [b]Department of Radiology and Radiological Science, Medical University of South Carolina, Charleston, SC 29425

Edited* by Leslie Greengard, New York University, New York, NY, and approved February 21, 2014 (received for review September 10, 2013)

Measuring molecular diffusion is widely used for characterizing materials and living organisms noninvasively. This characterization relies on relations between macroscopic diffusion metrics and structure at the mesoscopic scale commensurate with the diffusion length. Establishing such relations remains a fundamental challenge, hindering progress in materials science, porous media, and biomedical imaging. Here we show that the dynamical exponent in the time dependence of the diffusion coefficient distinguishes between the universality classes of the mesoscopic structural complexity. Our approach enables the interpretation of diffusion measurements by objectively selecting and modeling the most relevant structural features. As an example, the specific values of the dynamical exponent allow us to identify the relevant mesoscopic structure affecting MRI-measured water diffusion in muscles and in brain, and to elucidate the structural changes behind the decrease of diffusion coefficient in ischemic stroke.

A macroscopically uniform sample of a biological tissue, porous rock, or composite material appears incredibly complex at the mesoscopic scale. This scale, typically of the order ~ 0.1 to 10 μm, is intermediate between the microscopic scale of molecular dimensions, where material properties such as the local diffusion coefficient originate, and the macroscopic sample dimensions or imaging resolution. Quantifying the mesoscopic complexity noninvasively is important in the physical sciences for characterizing artificial and natural samples, and in the life sciences for diagnosing diseases, such as stroke and Alzheimer's, that manifest themselves at a cellular level.

Measuring molecular diffusion, e.g., of water, in such media has emerged as a universal noninvasive structural probe (1–8). Obtained with techniques ranging from single-molecule tracking (3) to diffusion-weighted MRI (dMRI) (4), macroscopic diffusion metrics are sensitive to the nominally invisible micron-level sample architecture, thanks to the diffusion length, i.e., the rms molecular displacement $L(t)=\langle \delta x^2(t)\rangle^{1/2}$, providing the mesoscopic length scale. However, a challenging ill-posed problem (1, 2, 9) has long been to quantitatively interpret a bulk diffusion measurement, i.e., to convert this manifestly sensitive metric into specific mesoscopic structural parameters, such as geometric properties of pores or biophysical parameters of cells.

Characterizing structure below a nominally achievable imaging resolution requires a structural model that predicts the result of the bulk measurement; by comparing the measurement to the prediction, the model parameters may be quantified. At the most basic level, a model is a rough sketch which captures the most essential parts of the structural complexity while neglecting the rest. Given the inherently irregular, or disordered nature of most specimens, a key challenge is to adequately and parsimoniously represent structural disorder.

Here we advocate that there are only a handful of qualitatively distinct ways to draw such sketches. More formally, we classify media based on the distinct types of long-range spatial correlations at the mesoscale, which we call "structural universality classes" (Figs. 1 and 2). The concept of universality is borrowed from statistical physics. In our context, it signifies the global similarity between different structurally complex samples that emerges at large distances whenever samples are sufficiently coarse-grained, such that local differences between members of each class become inessential. Technically, a universality class is determined via the two-point structure correlation function $\Gamma(r)$, in terms of the value of the structural exponent p in the $\Gamma(k)|_{k\to 0}\sim k^p$ behavior of its spatial Fourier transform $\Gamma(k)$ (Figs. 1 and 2).

Remarkably, we find that the most basic diffusion metrics, such as the velocity autocorrelation function and the time-dependent diffusion coefficient, can distinguish between the structural universality classes, based on the key relation

$$\vartheta=(p+d)/2 \qquad [1]$$

(*Materials and Methods*; see also *SI Text, Section I* and Fig. S1). The relation **1** between the dynamical exponent ϑ characterizing diffusion in the long-time limit, and the structural exponent p which determines the structural universality class in d spatial dimensions, relates the measurement and the structure, and allows one to determine the most appropriate kind of model based on the measurement. By using our framework, we identify the relevant mesoscopic structure affecting water diffusion measured with MRI in muscles and in brain, and elucidate the corresponding mesoscopic changes providing clinically relevant dMRI contrast in ischemic stroke.

The relation **1** expresses an idea that molecular diffusion at long time t, i.e., large diffusion length $L(t)$, preserves the footprint of the underlying structural complexity. This footprint is reflected in the exponent ϑ describing the decay of the temporal correlations (memory) in the molecular velocity autocorrelation function

Significance

A major challenge in the physical and life sciences is to see the invisible by quantifying the structure of materials and living tissues below nominal imaging resolution. Measurement of molecular diffusion performed at a macroscopic level is a common noninvasive structural probe. Interpreting its results involves identifying which structural features, out of a myriad of parameters, most strongly affect the diffusion coefficient. Here we address this ill-posed problem by classifying media into a relatively small number of universality classes, based on the nature of long-range structural correlations. We show that the time dependence of a macroscopic diffusion coefficient distinguishes between these classes. Using this approach, we identify dominant restrictions to MRI-measured water diffusion in muscles and in cortical gray matter.

Author contributions: D.S.N., J.H.J., J.A.H., and E.F. designed research; D.S.N. performed analytical calculations; E.F. performed numerical calculations; D.S.N., J.H.J., J.A.H., and E.F. performed research; D.S.N. and E.F. analyzed data; and D.S.N. wrote the paper.

The authors declare no conflict of interest.

*This Direct Submission article had a prearranged editor.

[1]To whom correspondence should be addressed. E-mail: dima@alum.mit.edu.

This article contains supporting information online at www.pnas.org/lookup/suppl/doi:10.1073/pnas.1316944111/-/DCSupplemental.

$$\mathcal{D}(t) \equiv \langle v(t)v(0)\rangle \sim t^{-(1+\vartheta)}, \qquad \vartheta > 0. \qquad [2]$$

Practically, the power law tail **2** can be identified in the way the time-dependent instantaneous diffusion coefficient

$$D_{\text{inst}}(t) \equiv \frac{\partial}{\partial t}\frac{\langle \delta x^2\rangle}{2} = \int_0^t \mathrm{d}t'\ \mathcal{D}(t') \simeq D_\infty + \text{const}\cdot t^{-\vartheta} \qquad [3]$$

approaches the finite bulk diffusion constant D_∞. The quantity $D_{\text{inst}}(t)$ is accessible with techniques (3, 4) measuring the mean-square molecular displacement $\langle \delta x^2(t)\rangle$ in a particular direction (Eqs. **4–6**).

The relation **1** provides a way to determine the exponent p and, thereby, the structural universality class, using bulk diffusion measurement. Local properties may affect the coefficients, e.g.,

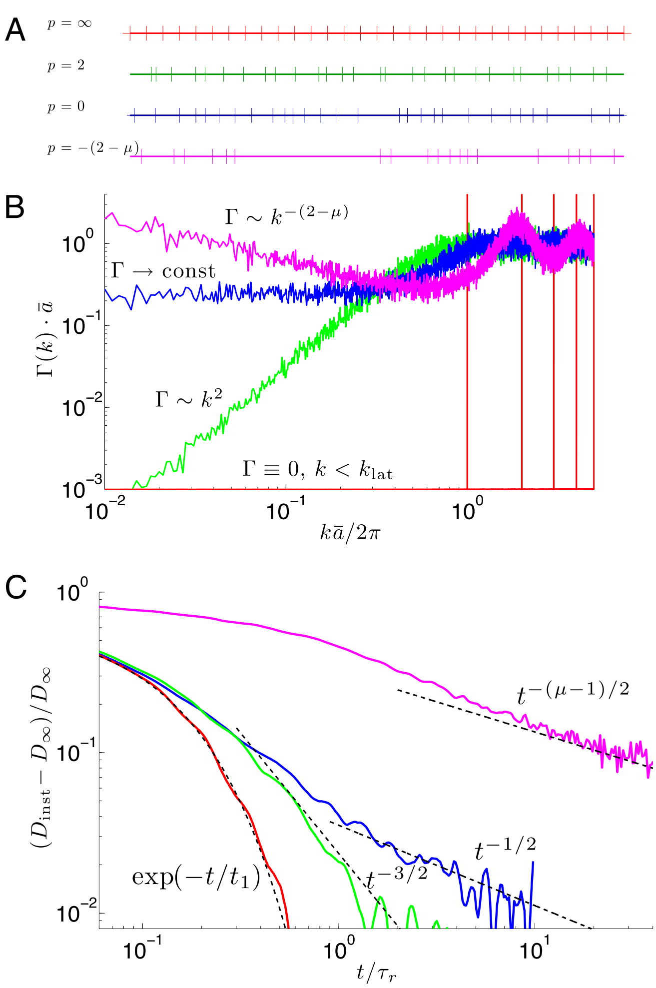

Fig. 1. Time-dependent diffusion distinguishes between structural universality classes in one dimension, represented here by the placement of identical permeable barriers with the same mean density. (*A*) Order (red), hyperuniform disorder (green), short-range disorder (blue), and strong disorder (magenta) are shown. (*B*) The barrier densities have qualitatively different large-scale fluctuations, reflected in the small-k behavior of their density correlator $\Gamma(k) \sim k^p$ (see *Examples of Structural Universality Classes*). (*C*) Numerical results confirming the relation **1**. The time-dependence **3** clearly distinguishes between the four arrangements, while the value D_∞ is the same for all of them. The dashed lines are the exact power laws from Eqs. **S14**, **S19**, and **S23**, and the exponential decrease is from the exact solution, Eq. **S25**. Strong disorder occurs for $1 < \mu < 2$; here $\mu = 7/4$.

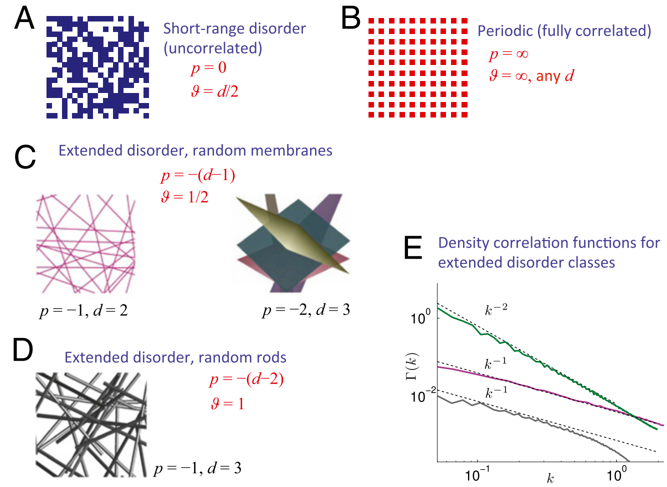

Fig. 2. Structural universality classes in dimension $d > 1$. (*A* and *B*) The examples of analogs of the $d = 1$ classes, corresponding to Fig. 1 (blue and red). (*C–E*) The extended universality classes inherent to $d > 1$. (*C*) Random membranes, with representatives shown for $d = 2$ and $d = 3$, result in $\vartheta = 1/2$ for any d. (*D*) Random rods, with a representative shown for $d = 3$, result in $\vartheta = 1$ for any d. (*E*) Structure correlator $\Gamma(k) \sim k^p$ (numerically calculated and angular averaged, arbitrary units) for *C* (magenta in $d = 2$ and green in $d = 3$), and for *D* (gray), exhibits the negative structural exponent $p = -d_s$.

the values of D_∞ and of the prefactor of $t^{-\vartheta}$ in **[3]**, but not the exponent ϑ. The latter is robust with respect to variations between samples of a similar origin, such as due to biological variability. This picture is akin to critical phenomena (10), where the phase transition temperature is nonuniversal (sensitive to short-scale details), while the critical exponents distinguish, based on global symmetries, between the universality classes of long-range fluctuations.

Examples of Structural Universality Classes

Fig. 1 illustrates how diffusion distinguishes between the universality classes via the relation **1** in the $d = 1$ dimension. The Monte Carlo (MC)-simulated diffusion is hindered by the permeable barriers with mean density $\bar n = 1/\bar a$ and permeability κ (*Materials and Methods*). The universality classes, realized here by the different ways of arranging the same 40,000 barriers (sample cutouts shown in Fig. 1*A*), exhibit distinct structural exponents p in the barrier density correlator (Fig. 1*B*), which result in the distinct exponents **1** (Fig. 1*C*).

Order. Any periodic arrangement (such as Fig. 1, red) is reflected in the Bragg peaks in $\Gamma(k)$, with $\Gamma \equiv 0$ for k below the minimal reciprocal lattice vector, formally corresponding to $p = \infty$. As the coarse-graining beyond the lattice constant does not increase the structural fluctuations, $\mathcal{D}(t)$ decays and $D_{\text{inst}}(t)$ reaches D_∞ exponentially fast, formally corresponding to $\vartheta = \infty$ (i.e., faster than any inverse power law); see also *SI Text, Section IIE*.

Structural disorder comes in qualitatively different ways.

Short-Range Disorder. Short-range disorder is arguably the most common disorder class, and it serves as a good reference point. It is characterized by a finite correlation length l_c, beyond which the correlator $\Gamma(r)$ decreases sufficiently fast, which corresponds to the finite plateau in $\Gamma(k)|_{k\to 0} = \text{const} > 0$, and the structural exponent $p = 0$, similar to the Poissonian disorder (uncorrelated restrictions). Finite correlation length means that, at larger distances, the variance of the number of restrictions scales in proportion to their mean number in a given volume, consistent with the central limit theorem. In Fig. 1 (blue), we chose each successive interval a_m between barriers independently from the distribution $P(a)$ with mean $\bar a = 1/\bar n$ and finite variance σ^2. This results in the finite plateau $\Gamma|_{k\to 0} = \sigma^2/\bar a^3$, as calculated in

SI Text, Section IIB. Hence, $\vartheta = 1/2$ (Fig. 1*C*). Likewise, in d dimensions, short-range disorder in the placement of local restrictions to diffusion would correspond to $\vartheta = d/2$, according to Eq. **1**.

Hyperuniform Disorder. Hyperuniform disorder (11, 12) is characterized by reduced long-range fluctuations, with the variance in the number of restrictions in a given domain increasing slower than the domain volume (sub-Poissonian statistics), reflected in $p > 0$ and $\vartheta > d/2$. In Fig. 1, we displaced the barriers from their positions in a regular lattice by independent random shifts leading to $\Gamma(k)|_{k\to 0} \sim k^2$, such that $p = 2$ (Fig. 1*B*), yielding $\vartheta = 3/2$ (Fig. 1*C*) according to **[1]**; see also *SI Text, Section IID*.

Strong Disorder. One can imagine an opposite situation of long-range fluctuations enhanced relative to the short-range disorder; let us call it "strong disorder." Structural fluctuations growing faster with volume than prescribed by the central limit theorem are reflected in a diverging $\Gamma|_{k\to 0}$, i.e., the exponent $p < 0$, such that $\Gamma(r) \sim 1/r^{p+d}$ decreases slower than $1/r^d$ in d dimensions. This would lead to the exponent $\vartheta < d/2$ (weak self-averaging). In Fig. 1 (magenta), we used the Levy (fat tail) distribution $P(a) \sim 1/a^{1+\mu}$ with $1 < \mu < 2$ for the successive barrier intervals, such that the mean interval is finite, but the variance $\langle (a-\bar{a})^2 \rangle_P$ diverges. Our choice of $\mu = 7/4$ yields $p = \mu - 2 = -1/4$ and $\vartheta = (\mu - 1)/2 = 3/8$ in agreement with Eq. **1** (see *SI Text, Section IIC* for derivation).

Higher Dimensions. As already indicated, the above universality classes are also present in higher dimensions $d > 1$. Short-range disorder in the placement of any kind of finite-size restrictions yields the structural exponent $p = 0$, leading to the short-range disorder in the (sufficiently coarse-grained) local diffusion coefficient $D(\mathbf{r})$, such as shown in Fig. 2*A* for $d = 2$. The short-range disorder in $D(\mathbf{r})$ yields (13, 14) the exponent $\vartheta = d/2$ in agreement with Eq. **1**. All ordered (periodic) arrangements of permeable or impermeable restrictions to diffusion in any d (e.g., Fig. 2*B*) are characterized by the vanishing $\Gamma(k)$ for sufficiently small k, formally corresponding to $p = \infty$, and yielding an exponentially fast decay of the memory in diffusion, $\vartheta = \infty$. (Paraphrasing ref. 15, ordered structures are all alike; every disorder class is disordered in its own way.) The hyperuniform disorder comes with different $p > 0$. When the restrictions are independently displaced away from the lattice sites, $p = 2$ in any d. The value $p \simeq 1$ occurs for a maximally random jammed state in $d = 3$ (12). We note that Eq. **1** provides a means to observe the jamming transition, from $p = 0$ at low packing density, to $p \simeq 1$, via measuring diffusion in-between packed hard spheres.

Extended Disorder Classes. These disorder classes (Fig. 2 *C* and *D*) are inherent to $d > 1$. They open up a natural way to realize strong disorder, with diverging $\Gamma(k)$ (Fig. 2*E*) corresponding to $p < 0$ and $\vartheta < d/2$ without a need to invoke a Levy distribution (as had to be done in Fig. 1). A negative p can be achieved by placing regular structural components (e.g., infinite lines, planes) with dimensionality $d_s < d$, in a random fashion, in which case $p = -d_s$ (a negative integer), the structural correlator $\Gamma(r) \sim 1/r^{d-d_s}$ decays slower than $1/r^d$, and 2ϑ corresponds to their codimension $d - d_s$. The first such example (16) is the extended disorder realized by random permeable hyperplanes, $d_s = d - 1$ (Fig. 2*C*), resulting in $\vartheta = 1/2$ in any d. Likewise, randomly placed and oriented rods, $d_s = d - 2$, embedded in $d = 3$ dimensions (Fig. 2*D*) would realize $p = -1$ and $\vartheta = 1 < 3/2$. For the structural components with finite extent l_c, the disorder becomes short-ranged, $p \to 0$ and $\vartheta \to d/2$, when the diffusion length exceeds their size (the correlation length l_c).

Generalizations and Discussion. The examples in Fig. 1 already demonstrate that selecting the right global sketch of mesoscopic structure is essential, and that diffusion measurement provides an objective way of doing so. This should be contrasted with comparing small fragments (e.g., Fig. 1*A*, blue and green); the hyperuniform fragment may as well seem locally more disordered than the short-ranged one. However, diffusion unequivocally determines that the large-scale fluctuations in the blue sample are qualitatively stronger than in the green one, leading to a slower decrease of $D_{\text{inst}}(t)$ (Fig. 1*C*), confirming the relation **1**.

Of course, from a long-time measurement it is impossible to deduce how exactly a given structural universality class is realized at short distances. Instead of thin barriers in Fig. 1, we could have chosen finite intervals with a different diffusion coefficient, or smooth variations of local diffusion coefficient $D(x)$, realizing the same low-k behavior of $\Gamma(k)$. Likewise, the lines, planes, or rods from Fig. 2 *C* and *D* could be structurally complex at short distances. The information deduced about the global organization should practically complement our knowledge about the mesoscopic structure and the dimensionality d, as illustrated in the subsequent in vivo examples.

Above, we assumed that the molecules (the random walkers) can spread everywhere. When impermeable boundaries split the space into disconnected parts, Eq. **1** applies separately to the contribution from each part, which then add up. The most relevant disorder contribution is the one with the smallest ϑ, yielding the slowest power law tails **2** and **3**.

Extended Disorder Provided by Muscle Fiber Walls

In Fig. 3, we analyze the time dependence of diffusion tensor eigenvalues in the fresh ex vivo muscle tissue samples measured by Kim et al. (17). The nondispersive eigenvalues λ_1 correspond to the unrestricted diffusion along the fibers. The transverse components $\lambda_\perp(t)$ in the $d = 2$ fiber cross-section (Fig. 3*C*) are strongly dispersive. Representing the data as function of $t^{-1/2}$, we observe the

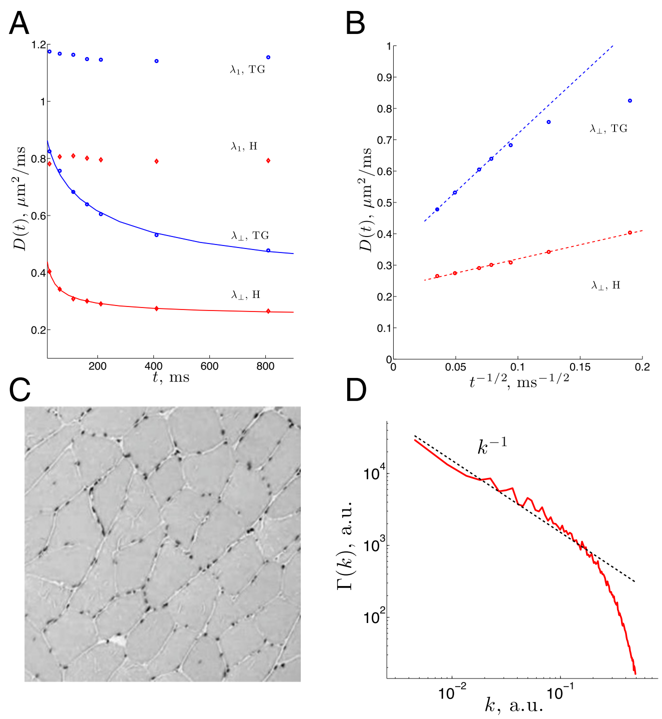

Fig. 3. Time-dependent diffusion transverse to muscle fibers from ref. 17 reveals extended structural disorder class of $d_s = 1$ in $d = 2$, provided by the muscle fiber membrane (sarcolemma). (*A*) The longitudinal, λ_1, and the transverse, $\lambda_\perp = (\lambda_2 + \lambda_3)/2$, diffusion tensor components for calf tongue genioglossus (TG) (blue circles) and heart (H) (red diamonds). Solid lines are the fit of $\lambda_\perp(t)$ to $D(t)$ derived from Eq. **S27** with $d = 2$. For fit results see Table S1. (*B*) Data for $\lambda_\perp(t)$ replotted as function of $t^{-1/2}$ consistent with $\vartheta = 1/2$. Eq. **1** yields $p = -1$; hence, $d_s = 1$ (see *Extended Disorder Provided by Muscle Fiber Walls* and Fig. 2*C*). (*C*) Muscle slice across the fibers. (*D*) $\Gamma(k)$ calculated from image intensity in *C*. Tight cell packing achieved by straight cell walls in *C* results in exponent $p = -1$ of the extended disorder class of Fig. 2*C*, yielding $\vartheta = 1/2$.

asymptotic tail **3**. Indeed, the fit of $\lambda_\perp(t)$ to Eq. **5** yields $\vartheta \approx 0.5$ for both tongue and heart (Fig. S2), exemplifying weak self-averaging, $\vartheta < d/2$, in contrast to $\vartheta = 1$ expected for the $d = 2$ short-range disorder. We thus conclude that the restrictions to water diffusion are strongly spatially correlated on the scale of the diffusion length (up to ~ 30 μm in this measurement), which puts them into the extended disorder class of Fig. 2*C* with $d_s = 1$ in $d = 2$.

In *SI Text, Section III*, we argue that the relevant restrictions are in fact muscle cell membranes (sarcolemma), and quantify their permeability and cell size (Table S1). The good agreement between the fit parameters and histological values can be rationalized by comparing a typical histological slice transverse to muscle fibers (Fig. 3*C*) with the random barriers in two dimensions (Fig. 2*C*). Tight packing of muscle cells makes the fiber walls fairly flat and spatially correlated even over length scales exceeding typical fiber diameter, resulting in strong extended structural correlations, $\Gamma(k) \sim 1/k$, within the plane transverse to the fibers, as shown in Fig. 3*D* calculated from the intensity profile of Fig. 3*C*. Hence, the dynamical exponent **1** establishes the effect of permeable cell walls on the dMRI signal.

One-Dimensional Short-Range Disorder in the Brain

We now turn our focus to brain. An important early observation (18) is the almost twofold decrease in the water diffusion coefficient minutes after brain injury. Measured at times $t \sim 100$ ms when any residual time dependence in brain is small, the drop in the diffusion coefficient D_∞ is now used clinically as a noninvasive diagnostic marker for acute ischemia (19). However, the biophysical origin of this phenomenon has remained under debate for over two decades. A closely related challenge is to identify the dominant restrictions or cell mechanisms which determine water diffusion in healthy brain.

Here, we address these two related questions by focusing on the Fourier transform $\mathcal{D}(\omega)$ (Eq. **6**) of the velocity autocorrelation function **2** in rat cortical gray matter. We observe that the real part $\mathrm{Re}\,\mathcal{D}(\omega)$ measured by Does et al. (20) with oscillating gradients (4) exhibits the $\vartheta = 1/2$ dispersion (Fig. 4*A*) in the whole frequency range, $\omega/2\pi \le 0.5$ kHz, in a fairly isotropic brain region.

This value of ϑ is striking. It is different from the naive $\vartheta = 3/2$ for the fully random (uncorrelated) medium in $d = 3$ dimensions (similar to Fig. 2*A*). It tells that either the structure is highly correlated, $p = -2$ (such as in Fig. 2*C*) or the effective dimension of some tissue compartments is below 3 (which is favored anatomically; Fig. 4*B*). Another important observation is that the value $\vartheta = 1/2$ does not change following the onset of ischemia.

By identifying the $\vartheta = 1/2$ exponent, we reduce the problem of the origin of the diffusion slowdown in stroke, that could occur due to a myriad of reasons, to focusing on which structural changes affect the diffusion along randomly oriented narrow neurites (dendrites and axons). The effective dimension $d = 1$ is maintained by neurite walls; $\vartheta = 1/2$ yields $p = 0$, short-range disorder along the neurites (Fig. 4*B*), so that the universality class is that of Fig. 1 (blue). The extraneurite water contributes $\vartheta = 1$ (as in Fig. 2*D*) which is less relevant: since $|\omega|^1 + |\omega|^{1/2} \sim |\omega|^{1/2}$ as $\omega \to 0$, its effect in the dispersive $\mathrm{Re}\,\mathcal{D}(\omega)$ is overshadowed by that of intraneurite water. Our argument incidentally confirms that the neurites are effectively impermeable on the time scales relevant for the measurement (20). (Notable exchange would have destroyed the $d = 1$ contribution, yielding an overall $\vartheta = 1$, not supported by the data in Fig. 4*A*.)

The disorder, for the dendrites, may include spines, variations in thickness ("beads") and in local directionality on the ~ 1 μm scale (21); for the axons, the synaptic boutons (varicosities) separated (22) by 3 to 6 μm. Our short-range disorder prediction is remarkably consistent with the measured variance in the varicosity number within a window growing in proportion to the mean within this window (22), a defining signature of the $p = 0$ exponent. Ischemia causes beading, i.e., more pronounced varicosities in both dendrites and axons (23, 24), which is likely to increase the disorder. Any short-range disorder increase would cause the increase in the prefactor in the $\omega^{1/2}$ contribution to $\mathcal{D}(\omega)$ according to Eq. **7**, and the decrease in D_∞ (Eq. S7), both consistent with the data in Fig. 4*A*.

We underscore that it is focusing on the functional form of the dispersion, rather than on a single number D_∞, that allows us to clarify the origin of a complex biophysical phenomenon. Our approach validates the picture of neurites as effectively impermeable channels (25–28) and adds to it a crucial piece, the short-range disorder. The increase of disorder along neurites as a reason behind D_∞ decrease is consistent with the neurite beading shown to reduce D_∞ under a mechanical stress in parallel ex vivo axons (29), as well as with intraaxonal diffusion coefficient decrease in human stroke (30). Certainly, there could be factors other than beading that could add to the short-range disorder along neurites, and its increase in stroke. The $\vartheta = 1/2$ dispersion disfavors commonly discussed alternatives such as active streaming breakdown, swelling of cell bodies, and increase in the cytoplasmic viscosity as primary contributions to D_∞ decrease.

The present framework may stimulate more focused investigations of ischemic stroke, as well as of other neurological diseases. In particular, one may correlate the time- or frequency-dependent diffusion with morphological changes during status epilepticus and electrical activation (31) and severe hypoglycemia (32) also known to reduce the value of D_∞. The change in the number and morphology of neurite varicosities in Alzheimer's disease (33) should result in changes both in D_∞ and in the magnitude of the $\omega^{1/2}$ dispersion.

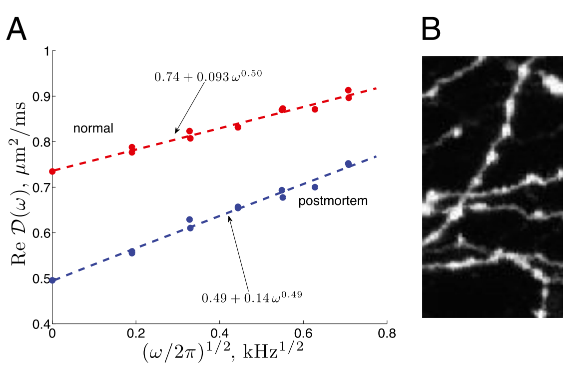

Fig. 4. Dispersive $\mathcal{D}(\omega)$ in cerebral gray matter consistent with $d = 1$ diffusion along narrow neurites in the presence of short-range disorder ($p = 0$), both in normal and globally ischemic rat brain. (*A*) Original data (20) for d-sin and cos gradient waveforms, fitted to Eq. **6**, yields $\vartheta = 0.50 \pm 0.07$ for normal and $\vartheta = 0.49 \pm 0.05$ for postmortem brain. The role of the disorder (the slope) increases after global ischemia onset. (*B*) Varicose axons from rat hippocampus area CA1 (22) rationalizing the picture of an effectively 1D diffusion inside narrow randomly oriented and structurally disordered neurites.

Conclusions

In this work, we have connected the dynamical exponent **1** to global structural organization, to study mesoscopic structure with noninvasive diffusion measurements. This framework is particularly useful for biological tissues. While biophysical parameters may vary strongly and continuously between samples, the exponent ϑ takes fixed values determined by the disorder universality class, and it is robust with respect to the biological variability. As a result, we have identified the dominant role of cell membranes restricting water motion in muscles, and have argued for an increase in the structural short-range disorder along the neurites as a cause of the diffusion coefficient decrease after ischemic stroke. We believe the proposed classification of structural disorder may help identify and quantify the dominant types of restrictions in other living tissues, as well as in diffusion or heat or electrical conduction in composite materials, porous media, and other structurally complex samples. Extending this classification to quantum (34) or wave (35) transport could tie rich physics of localization to the types of global structural organization at the mesoscale.

Materials and Methods

Diffusion Metrics. The fundamental quantity, the velocity autocorrelator **2**, is often difficult to measure directly. Instead, there exist a number of equivalent time- or frequency-dependent diffusion metrics, with relations between them described in refs. 36 and 37. To interpret various kinds of diffusion measurements, such as dMRI results (17, 20), here we outline how the power law tail **2** manifests itself in these metrics. We assume the sample to be statistically isotropic, so that the diffusion metrics are isotropic tensors, and the correlation functions depend on $r=|\mathbf{r}|$ and $k=|\mathbf{k}|$. Generalization to the anisotropic case presents no conceptual difficulty, but makes the presentation more cumbersome.

The instantaneous diffusion coefficient $D_{\mathrm{inst}}(t)$ defined in Eq. **3** is the natural metric to study structural correlations, as it quantifies how the spreading of a packet of random walkers is hindered by the mesoscopic structure at the time scale t. From our perspective, it is a perfect quantity to determine the exponent ϑ. However, this is not the most commonly used metric in practice.

The most commonly reported diffusion coefficient

$$D(t)\equiv\frac{\langle\delta x^2(t)\rangle}{2t}=\frac{1}{t}\int_0^t D_{\mathrm{inst}}(t')\mathrm{d}t' \qquad [4]$$

describes the dynamics of the cumulative, rather than instantaneous, mean-squared displacement along a particular direction $\hat{x}$ over the diffusion time t. This is the case both in the dMRI (4, 17) and in the direct molecular tracking techniques (3). This definition has a perceived advantage of dividing by time, rather than differentiating with respect to it; clearly, differentiating increases the noise, while dividing does not.

The definition **4** may mask the exponent ϑ. Indeed, its long t behavior

$$D(t)\simeq D_\infty+\mathrm{const}\cdot t^{-\tilde{\vartheta}},\quad \tilde{\vartheta}=\min\{\vartheta,1\}. \qquad [5]$$

In other words, for the tail **2** to be manifest in $D(t)$, it should be sufficiently slow, $\vartheta\le 1$, so that it is unaffected by the averaging over the increasing interval t in **[4]**. In the opposite case, $\vartheta>1$, the $t^{-\vartheta}$ term in $D_{\mathrm{inst}}(t)$ becomes subleading to the $1/t$ term from the integral in **[4]** converging at short t.

Hence, to practically determine the dynamical exponent ϑ, one could first check whether the fit to **[5]**, using the less noisy definition **4**, produces the value $\tilde{\vartheta}<1$. If it does (as in our example of diffusion transverse to muscle fibers), this is the true value of $\vartheta=\tilde{\vartheta}$. In the opposite case, the fit would yield the $1/t$ tail, $\tilde{\vartheta}=1$, which would mask the true value of $\vartheta>1$. Then, one must perform the differentiation $D_{\mathrm{inst}}(t)=\partial_t[tD(t)]$ and obtain ϑ from the fit to **[3]**, with the unfortunate effect of amplifying the measurement noise, as shown by comparing Figs. 1 and 5. Practically, this results in more stringent requirements on the signal-to-noise ratio and on the greater number of experimental time points.

There is another useful way of uncovering the exponent ϑ, as long as $\vartheta<2$, without the need to take a time derivative. The same power law tail

$$\mathrm{Re}\,\mathcal{D}(\omega)\equiv\frac{1}{2}\langle v_{-\omega}v_\omega\rangle\simeq D_\infty+\mathrm{const}\cdot|\omega|^\vartheta,\quad \omega\to 0, \qquad [6]$$

persists in the dispersive diffusivity $\mathcal{D}(\omega)\equiv\int_0^\infty \mathrm{d}t\, e^{i\omega t}\mathcal{D}(t)$, which is the Fourier transform of the retarded velocity autocorrelator **2**. The physical meaning of $\mathcal{D}(\omega)$ is in relating the current $J_{\omega,\mathbf{r}}=-\mathcal{D}(\omega)\nabla_{\mathbf{r}}\psi_{\omega;\mathbf{r}}$ of the random walkers to their density gradient (36), somewhat similar to the dispersive electrical

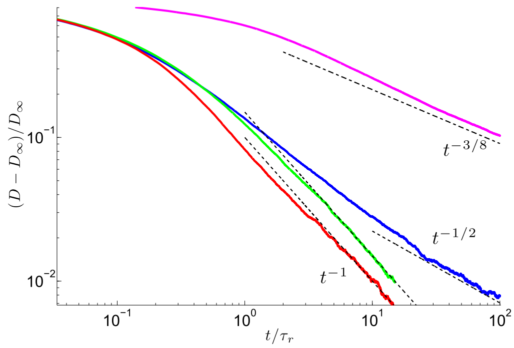

Fig. 5. Cumulative diffusion coefficient, Eq. **4**, for the 1D example of Fig. 1. Dashed lines correspond to the asymptotic power law decrease of $D(t)$. For $\vartheta=1/2$ and $\vartheta=3/8$ (blue represents short-range disorder and magenta strong disorder), the power law in $D(t)$ coincides with that in $D_{\mathrm{inst}}(t)$ (in accord with Eq. **5**) whereas for $\vartheta>1$ (red represents periodic and green hyperuniform), it is masked by the $1/t$ term. Taking the derivative $D_{\mathrm{inst}}=\partial_t(tD(t))$ reveals the values of ϑ (as shown in Fig. 1) but increases noise.

conductivity; it defines the pole of the diffusion propagator (see refs. 13, 14, 16, 36, and 37 and also the discussion in *SI Text, Section I*). Fortunately, there exists a dMRI measurement protocol, the oscillating gradient technique (4, 20), which directly measures (37) $\mathrm{Re}\,\mathcal{D}(\omega)$. This is the quantity used in the example of diffusion in cerebral gray matter (Fig. 4).

Derivation of Eq. 1: Homogenization. In this work, we consider the most widespread situation, when a sample has a nonzero macroscopic diffusion constant $D_\infty\equiv[\langle\delta x^2\rangle/2t]_{t\to\infty}$, i.e., the diffusion asymptotically becomes normal, or Gaussian. A well-defined macroscopic D_∞, observed in an overwhelmingly broad variety of mesoscopically heterogeneous samples, attests to the robustness of the diffusion as a Gaussian fixed point with respect to adding the structural complexity (disorder). In this case, a macroscopic sample represents the disorder ensemble, i.e., the system is self-averaging (38). Conversely, the absence of D_∞, e.g., for fractals, near a percolation threshold (2, 39), or for random drifts in one dimension (40, 41), signifies the so-called anomalous diffusion (2) not considered here.

The general relation of the long-time behavior **2** and **3** to the mesoscopic structure rests on the homogenization argument: at long diffusion time t, the sample, as seen by random walkers traveling over a growing diffusion length $L(t)\equiv\langle\delta x^2(t)\rangle^{1/2}\simeq\sqrt{2D_\infty t}$, appears increasingly more uniform due to self-averaging. The sample is being effectively coarse-grained over $L(t)$, such that the strong mesoscopic heterogeneity is gradually forgotten, and the deviation $\delta D(\mathbf{r})=D(\mathbf{r})-D_\infty$ of the smoothly varying coarse-grained diffusion coefficient $D(\mathbf{r})$ from D_∞ becomes small. This justifies calculating the self-energy part of the disorder-averaged diffusion propagator only to the lowest (second) order in the variable component $\delta D(\mathbf{r})$. Eventually, the perturbative treatment around D_∞ becomes asymptotically exact (as discussed in *SI Text, Section I* and Fig. S1) and the (small) deviation

$$\frac{\mathcal{D}(\omega)-D_\infty}{D_\infty}\simeq-\frac{i\omega}{D_\infty^2 d}\int\frac{\mathrm{d}^d\mathbf{k}}{(2\pi)^d}\frac{\Gamma_D(k)}{-i\omega+D_\infty k^2} \qquad [7]$$

is given in terms of the Fourier transform $\Gamma_D(k)=\int\mathrm{d}^d\mathbf{r}\; e^{-i\mathbf{kr}}\;\Gamma_D(r)$ of the two-point correlation function $\Gamma_D(r)=\langle\delta D(\mathbf{r}_0+\mathbf{r})\delta D(\mathbf{r}_0)\rangle$ in d spatial dimensions. Using the relation between $\mathcal{D}(\omega)$ and $D_{\mathrm{inst}}(t)$,

$$D_{\mathrm{inst}}(t)=\int\frac{\mathrm{d}\omega}{2\pi}e^{-i\omega t}\frac{\mathcal{D}(\omega)}{-i(\omega+i0)} \qquad [8]$$

(which can be derived using the cumulant expansion; cf. ref. 36), we obtain

$$D_{\mathrm{inst}}(t)-D_\infty\simeq\frac{1}{dD_\infty}\int\frac{\mathrm{d}^d\mathbf{k}}{(2\pi)^d}\Gamma_D(k)e^{-D_\infty k^2 t}. \qquad [9]$$

Equivalently, the last equation can be recast in the form

$$D_{\mathrm{inst}}(t)\simeq D_\infty+\frac{1}{dD_\infty}\cdot\langle(\delta D)^2\rangle\big|_{L(t)}, \qquad [10]$$

where $\langle(\delta D)^2\rangle\big|_L$ is the variance of the Gaussian-smoothed values $\delta D(\mathbf{r})|_L=\int\mathrm{d}^d\mathbf{r}'\,\delta D(\mathbf{r}+\mathbf{r}')e^{-r'^2/L^2}\big/(\pi L^2)^{d/2}$. In other words, the diffusion effectively applies a low-pass filter $e^{-k^2L^2/4}$ to the Fourier components of $D(\mathbf{r})$ and, thus, to its correlator $\Gamma_D(k)$, admitting harmonics with progressively smaller wavenumbers $k\lesssim 1/L(t)$. As the variance $\langle(\delta D)^2\rangle\big|_L\sim L^{-2\vartheta}$ decreases due to the smoothing, the measured diffusion coefficient $D_{\mathrm{inst}}(t)$ monotonically decreases toward D_∞. The power law exponent **1** is then directly related to the dimensionality d and to the exponent p which determines the $k\to 0$ behavior of $\Gamma_D(k)\sim k^p$.

We are interested in the spatial correlations $\Gamma(r)=\langle n(\mathbf{r}_0+\mathbf{r})n(\mathbf{r}_0)\rangle$ of the underlying mesoscopic structure $n(\mathbf{r})$ responsible for the heterogeneity of $D(\mathbf{r})$. Depending on the sample, $n(\mathbf{r})$ may stand for the density of grains, barriers, and other structural components that restrict diffusion (e.g., Figs. 1 and 2). This density is often strongly heterogeneous at the microscopic scale. Certainly, the coarse-grained $D(\mathbf{r})$ is not equal to the local average of the strongly varying microscopic diffusion coefficient caused by $n(\mathbf{r})$. However, the statistics of the large scale fluctuations of $n(\mathbf{r})$ asymptotically approaches that of the coarse-grained $D(\mathbf{r})$, such that for $k\to 0$

$$\Gamma_D(k)\simeq C(\bar{n})\cdot\Gamma(k),\quad C(\bar{n})=(\partial D_\infty/\partial\bar{n})^2. \qquad [11]$$

This asymptotically local relation rests on the self-averaging assumption which ensures the smooth dependence $D_\infty(\bar{n})$ on the sample mean $\bar{n}=\langle n(\mathbf{r})\rangle$ of the restrictions. Hence, after coarse-graining, a typical small local fluctuation $\delta D(\mathbf{r})\simeq(\partial D_\infty/\partial\bar{n})\delta n(\mathbf{r})$ becomes asymptotically proportional to the typical small local fluctuation $\delta n(\mathbf{r})=n(\mathbf{r})-\bar{n}$, as long as the self-averaging assumption holds. (Conversely, singular dependence $D_\infty(\bar{n})$, e.g., at the percolation threshold, is associated with the lack of self-averaging.) In this way, the exponent p characterizes long-range correlations in the sample's mesoscopic structure, $\Gamma(k) \sim \Gamma_D(k) \sim k^p$, and becomes accessible with a time-dependent diffusion measurement via the relation **1**.

Strong self-averaging in d dimensions occurs when the variance $\langle(\delta D)^2\rangle\big|_L$ decreases as the inverse diffusion volume L^{-d}, such as for short-ranged disorder ($p=0$), or faster, as for order or hyperuniform disorder ($p>0$). Weak self-averaging corresponds to the decrease $\sim L^{-2\vartheta}$ with a smaller power, $0<\vartheta<d/2$. For $p \le -d$, very strong fluctuations destroy self-averaging, a sample does not represent a disorder ensemble, the macroscopic D_∞ is undefined, and the present approach fails. Diffusion becomes anomalous (2), with mean-squared displacement $\langle\delta x^2(t)\rangle \sim t^{2/z}$ as $t\to\infty$ characterized by the dynamical exponent $z\ne 2$ (see, e.g., refs. 39–41).

MC Dynamics. For each disorder class in Figs. 1 and 5, MC simulated random walks of 4×10^6 random walkers evenly split between 40 disorder realizations of $N=1{,}000$ barriers each, were used to average $\langle\delta x^2\rangle$ over the paths and over the ensemble. The total length of each realization could be either smaller or larger than $N\bar{a}$ since barrier intervals were random (as described in *SI Text, Section II*). The trajectory of each random walker was a sequence of moves in a randomly chosen direction over a distance $dx=\sqrt{2D_0 dt}=0.008\ \bar{a}$ during a time step dt, where D_0 is the unrestricted (free) diffusion constant. This choice of $dx \ll \bar{a}$ ensured that the free diffusion was well simulated within each interbarrier interval, i.e., the effects of the finite step dx at the scale of interbarrier separation were already negligible. In this way, the added barriers can be viewed as restrictions, or "disorder," for the free 1D diffusion.

The barrier permeability κ (the dimensions of velocity) determines the dimensionless disorder strength (16),

$$\zeta=\bar{n}D_0/\kappa, \quad \bar{n}=1/\bar{a}. \qquad [12]$$

Keeping the same $\bar{a}$, D_0, and κ for all disorder classes yields the same macroscopic diffusion constant

$$D_\infty(\bar{n})=\frac{D_0}{1+\bar{n}D_0/\kappa}\equiv\frac{D_0}{1+\zeta}, \qquad [13]$$

an exact result in $d=1$ irrespective of the barrier placement (16, 42). As an illustration, in Fig. 1 we chose $\zeta=1$, which yields $D_\infty=D_0/2$, for all disorder classes. Incidentally, in tissues often $\zeta\sim1$ (see, e.g., Table S1).

Transmission across a barrier occurred with probability $\propto \kappa dx/D_0 \ll 1$ (43). The total diffusion time was $100\tau_r$, corresponding to a maximum of 1.5625×10^6 time steps per random walker, where

$$\tau_r=V/\kappa S\equiv\bar{a}/2\kappa \qquad [14]$$

is the mean residence time within an average interbarrier interval characterized by its surface-to-volume ratio $S/V=2/\bar{a}$. The MC results were carefully verified to yield the exact result for D_∞ (with better than 1% accuracy), as well as using the exact result for $D_{inst}(t)$ for the periodic barriers (comparing Eq. **S25** and the red curve in Fig. 1*C*). The random walk simulator was developed in C++. Simulations were carried on the New York University General Cluster, using 120 central processing unit cores simultaneously, within a total time of about 10 h per each disorder class.

To obtain $D_{inst}(t)$ in Fig. 1, the time derivative in Eq. **3** was calculated using the Savitzky–Golay smoothing procedure written in Matlab (MathWorks), with the sixth order polynomial interpolation over a window increasing with t to suppress the MC noise that becomes relatively more pronounced at longer diffusion times.

ACKNOWLEDGMENTS. We thank Sungheon Kim, Valerij Kiselev, and Daniel Sodickson for discussions; and New University–Information Technology Services for providing computational resources. Research was supported by the Raymond and Beverly Sackler Laboratories for Convergence of Physical, Engineering, and Biomedical Sciences; the Litwin Foundation for Alzheimer's Research; and the National Institutes of Health (1R01AG027852).

1. Haus JW, Kehr KW (1987) Diffusion in regular and disordered lattices. *Phys Rep* 150(5-6):263–406.
2. Bouchaud JP, Georges A (1990) Anomalous diffusion in disordered media: Statistical mechanisms, models and physical applications. *Phys Rep* 195(4-5):127–293.
3. Kusumi A, et al. (2005) Paradigm shift of the plasma membrane concept from the two-dimensional continuum fluid to the partitioned fluid: High-speed single-molecule tracking of membrane molecules. *Annu Rev Biophys Biomol Struct* 34:351–378.
4. Callaghan PT (1991) *Principles of Nuclear Magnetic Resonance Microscopy* (Clarendon, Oxford).
5. Mitra PP, Sen PN, Schwartz LM, Le Doussal P (1992) Diffusion propagator as a probe of the structure of porous media. *Phys Rev Lett* 68(24):3555–3558.
6. Latour LL, Svoboda K, Mitra PP, Sotak CH (1994) Time-dependent diffusion of water in a biological model system. *Proc Natl Acad Sci USA* 91(4):1229–1233.
7. Le Bihan D, ed (1995) *Diffusion and Perfusion Magnetic Resonance Imaging* (Raven, New York).
8. Mair RW, et al. (1999) Probing porous media with gas diffusion NMR. *Phys Rev Lett* 83(16):3324–3327.
9. Kac M (1966) Can one hear the shape of a drum? *Am Math Mon* 73:1–23.
10. Hohenberg PC, Halperin BI (1977) Theory of dynamic critical phenomena. *Rev Mod Phys* 49(3):435–479.
11. Torquato S, Stillinger FH (2003) Local density fluctuations, hyperuniformity, and order metrics. *Phys Rev E Stat Nonlin Soft Matter Phys* 68(4):041113.
12. Donev A, Stillinger FH, Torquato S (2005) Unexpected density fluctuations in jammed disordered sphere packings. *Phys Rev Lett* 95(9):090604.
13. Ernst MH, Machta J, Dorfman JR, van Beijeren H (1984) Long-time tails in stationary random media. 1. Theory. *J Stat Phys* 34(3–4):477–495.
14. Visscher PB (1984) Universality in disordered diffusive systems: Exact fixed-points in 1,2, and 3 dimensions. *Phys Rev B* 29(10):5472–5485.
15. Tolstoy L (1954) *Anna Karenina*, ed trans Edmonds R (Penguin Classics, Harmondsworth, UK).
16. Novikov DS, Fieremans E, Jensen JH, Helpern JA (2011) Random walk with barriers. *Nat Phys* 7(6):508–514.
17. Kim S, Chi-Fishman G, Barnett AS, Pierpaoli C (2005) Dependence on diffusion time of apparent diffusion tensor of ex vivo calf tongue and heart. *Magn Reson Med* 54(6):1387–1396.
18. Moseley ME, et al. (1990) Early detection of regional cerebral ischemia in cats: Comparison of diffusion- and T2-weighted MRI and spectroscopy. *Magn Reson Med* 14(2):330–346.
19. Adams HP, Jr., et al.; American Heart Association/American Stroke Association Stroke Council; American Heart Association/American Stroke Association Clinical Cardiology Council; American Heart Association/American Stroke Association Cardiovascular Radiology and Intervention Council; Atherosclerotic Peripheral Vascular Disease Working Group; Quality of Care Outcomes in Research Interdisciplinary Working Group (2007) Guidelines for the early management of adults with ischemic stroke. *Circulation* 115(20):e478–e534.
20. Does MD, Parsons EC, Gore JC (2003) Oscillating gradient measurements of water diffusion in normal and globally ischemic rat brain. *Magn Reson Med* 49(2):206–215.
21. García-López P, García-Marín V, Freire M (2006) Three-dimensional reconstruction and quantitative study of a pyramidal cell of a Cajal histological preparation. *J Neurosci* 26(44):11249–11252.
22. Shepherd GMG, Raastad M, Andersen P (2002) General and variable features of varicosity spacing along unmyelinated axons in the hippocampus and cerebellum. *Proc Natl Acad Sci USA* 99(9):6340–6345.
23. Zhang S, Boyd J, Delaney K, Murphy TH (2005) Rapid reversible changes in dendritic spine structure in vivo gated by the degree of ischemia. *J Neurosci* 25(22):5333–5338.
24. Li P, Murphy TH (2008) Two-photon imaging during prolonged middle cerebral artery occlusion in mice reveals recovery of dendritic structure after reperfusion. *J Neurosci* 28(46):11970–11979.
25. Behrens TEJ, et al. (2003) Characterization and propagation of uncertainty in diffusion-weighted MR imaging. *Magn Reson Med* 50(5):1077–1088.
26. Assaf Y, Freidlin RZ, Rohde GK, Basser PJ (2004) New modeling and experimental framework to characterize hindered and restricted water diffusion in brain white matter. *Magn Reson Med* 52(5):965–978.
27. Kroenke CD, Ackerman JJH, Yablonskiy DA (2004) On the nature of the NAA diffusion attenuated MR signal in the central nervous system. *Magn Reson Med* 52(5):1052–1059.
28. Jespersen SN, Kroenke CD, Østergaard L, Ackerman JJH, Yablonskiy DA (2007) Modeling dendrite density from magnetic resonance diffusion measurements. *Neuroimage* 34(4):1473–1486.
29. Budde MD, Frank JA (2010) Neurite beading is sufficient to decrease the apparent diffusion coefficient after ischemic stroke. *Proc Natl Acad Sci USA* 107(32):14472–14477.
30. Hui ES, et al. (2012) Stroke assessment with diffusional kurtosis imaging. *Stroke* 43(11):2968–2973.
31. Prichard JW, Zhong JH, Petroff OAC, Gore JC (1995) Diffusion-weighted NMR imaging changes caused by electrical activation of the brain. *NMR Biomed* 8(7-8):359–364.
32. Hasegawa Y, et al. (1996) Severe transient hypoglycemia causes reversible change in the apparent diffusion coefficient of water. *Stroke* 27(9):1648–1655, discussion 1655–1656.
33. Ikonomovic MD, et al. (2007) Superior frontal cortex cholinergic axon density in mild cognitive impairment and early Alzheimer disease. *Arch Neurol* 64(9):1312–1317.
34. Anderson PW (1958) Absence of diffusion in certain random lattices. *Phys Rev* 109:1492–1505.
35. Florescu M, Torquato S, Steinhardt PJ (2009) Designer disordered materials with large, complete photonic band gaps. *Proc Natl Acad Sci USA* 106(49):20658–20663.
36. Novikov DS, Kiselev VG (2010) Effective medium theory of a diffusion-weighted signal. *NMR Biomed* 23(7):682–697.
37. Novikov DS, Kiselev VG (2011) Surface-to-volume ratio with oscillating gradients. *J Magn Reson* 210(1):141–145.
38. Aharony A, Harris AB (1996) Absence of self-averaging and universal fluctuations in random systems near critical points. *Phys Rev Lett* 77(18):3700–3703.
39. Havlin S, Ben-Avraham D (2002) Diffusion in disordered media. *Adv Phys* 51:187–292.
40. Sinai YG (1970) Dynamical systems with elastic reflections. *Russ Math Surv* 25:137–189.
41. Havlin S, Schwartz M, Blumberg Selinger R, Bunde A, Stanley HE (1989) Universality classes for diffusion in the presence of correlated spatial disorder. *Phys Rev A* 40(3):1717–1719.
42. Crick F (1970) Diffusion in embryogenesis. *Nature* 225(5231):420–422.
43. Fieremans E, Novikov DS, Jensen JH, Helpern JA (2010) Monte Carlo study of a two-compartment exchange model of diffusion. *NMR Biomed* 23(7):711–724.